Journal of Medical Ultrasonics (2022) 49:569–578
https://doi.org/10.1007/s10396-022-01235-1

ORIGINAL ARTICLE–PHYSICS & ENGINEERING

Assessment of the frequency dependence of acoustic properties on material, composition, and scatterer size of the medium

Mai Ino[1] · Kenji Yoshida[2] · Shinnosuke Hirata[2] · Kazuyo Ito[3,4] · Tadashi Yamaguchi[2]

Received: 14 February 2022 / Accepted: 21 May 2022 / Published online: 13 September 2022

Abstract

Purpose The aim of this study was to elucidate the frequency dependence of the speed of sound (SoS) and attenuation coefficients in phantoms with controlled attenuation properties (scatterer density, scatterer size, absorption control material) and rat livers.

Methods The frequency dependence of SoS and attenuation coefficients were evaluated with ultrasound (1–15 MHz) by observing multiple phantoms with different scatterer sizes, densities, and presence or absence of evaporated milk as absorbing media. Normal and fatty model rat livers were examined with the same protocol.

Results The phantom results revealed that the scatterer density and SoS of the base media were the dominant factors causing the changes in SoS. Frequency dependence was not observed in SoS. Assessment of the attenuation coefficient showed that the frequency dependence was mainly affected by absorption attenuation when the scatterer was as small as a hepatocyte (i.e. ≤ 10 μm). Scattering attenuation was also observed to affect frequency dependence when the scatterer was as large as lipid droplets (i.e. ≤ 40 μm).

Conclusion Assuming a consistent size of the main scatterers in the evaluation medium, the frequency dependence of the SoS and attenuation coefficients may provide insight into the scatterer density and the contribution of absorption and scattering attenuation. Further studies in the higher frequency band (up to about 50 MHz) are expected to advance the clinical application of high-frequency ultrasound.

Keywords Speed of sound · Attenuation coefficient · Frequency dependence · Fatty liver · Quantitative ultrasound

Introduction

Ultrasound imaging is widely used to investigate disease progression because it is noninvasive, non-ionizing, and low-cost compared to other medical imaging modalities. However, diagnosis with ultrasound B-mode images greatly depends on the clinician's experience and their image reading skill. This also causes low reproducibility of observations due to its subjectiveness. Hence, there has been a great need for quantification in ultrasound imaging in clinical practice.

Quantitative ultrasound (QUS) methods have been developed for over 30 years [1]. For example, elasticity imaging called shear wave elastography (SWE) quantifies mechanical properties of soft tissues by estimating the shear wave propagation speed [2]. This method has shown promising results for staging liver fibrosis progression [3–5] and differentiating malignant lesions in breast cancer [6, 7]. Backscattered ultrasound spectrum analysis

✉ Mai Ino
m_ino@chiba-u.jp

✉ Tadashi Yamaguchi
yamaguchi@faculty.chiba-u.jp

1 Graduate School of Science and Engineering, Chiba University, 1-33 Yayoicho, Inage, Chiba 2638522, Japan

2 Center for Frontier Medical Engineering, Chiba University, 1-33 Yayoicho, Inage, Chiba 2638522, Japan

3 Institute of Engineering, Tokyo University of Agriculture and Technology, 2-24-16 Nakacho, Koganei, Tokyo 1848588, Japan

4 Singapore Eye Research Institute, Singapore National Eye Centre, Duke-NUS Medical School, The Academia, 20 College Road, Discovery Tower Level 6, Singapore 169856, Singapore

[8–10] and envelope statistics [11–18] have shown promise for soft tissue characterization. These QUS methods quantify microstructure-related tissue parameters based on backscattered echo signal data. Despite its quantifiability, differentiation of minute lesions and quantification of complex material remain challenging. For example, a human liver with fibrosis is composed of softer tissues such as hepatic cells and harder tissues such as fibers. The mixture of various tissues causes complicated ultrasound propagation due to various phenomena such as scattering, attenuation, reflection, and refraction. In another example, the amount of fat deposition and its distribution in the fatty liver is the key, but it is tough to diagnose using ultrasound B-mode images. QUS has been used to successfully differentiate fatty liver from normal liver [19–24], but accuracy is still insufficient to detect early fatty liver when the fat deposition level is less than 5% even with these methods. Understanding tissue-specific acoustic properties such as speed of sound (SoS), attenuation, and acoustic impedance at the micrometer scale is expected to improve the accuracy of these QUS techniques [25].

SoS and attenuation coefficients are among the most basic parameters in QUS [26–29]. However, only a few studies have been conducted to systematically evaluate them either with actual tissue or by means of verification studies [30–33]. In particular, regarding the estimation of attenuation coefficients, most of the studies assumed only absorption attenuation or did not consider absorption and scattering attenuation separately. This experimental study was conducted to examine how acoustic properties were estimated under a mixture of media with dominantly either scattering or absorption coefficient. This paper specifically discusses the frequency dependence of the SoS and attenuation coefficients for materials with experimentally controlled scatterer size, its density, and absorption attenuation. In particular, this paper discusses the contributions of the scatterer size and density of the material on estimated SoS, and the association between estimated attenuation coefficients and the experimentally controlled scattering attenuation and absorption attenuation of the media.

This paper consists of two independent experiments. The first experiment was the assessment of SoS and the attenuation coefficients of homogeneous phantoms adjusted with different scatterer sizes and densities, or different absorption attenuation coefficients, in the frequency band of 1–15 MHz. The phantom experiments aimed to verify the consistency with the theory of the effects of scatterer size and medium differences on acoustic properties. The second assessment was the examination of the acoustic properties of enucleated livers from a normal and fatty rat model. This experiment aimed to evaluate the frequency dependence of the acoustic properties with different tissue pathologies.

Materials and methods

Tissue-mimicking phantoms

Nine agar-based tissue-mimicking phantoms with a homogeneous scatterer distribution were created for this study (Supplementary Table 1). The phantom was made of 2 wt% agar (A1296; Sigma-Aldrich, MO, USA), degassed purified water, and spherical nylon scatterers. Each phantom was molded in a rectangular acrylonitrile–butadiene–styrene case (width × length × height = 40 mm × 40 mm × 6 mm). Scatterer diameter and the density of the phantom were controlled by the diameter (mean diameter of 10 µm (phantoms I to III, ORGASOL, 2002 EXD NAT 1; Arkema, Colombes, France) or 40 µm (phantoms IV to VI, ORGASOL, 2002 ES4 NAT 3; Arkema, Colombes, France)) and density of the spherical nylon scatterers (0.5, 1.5, or 5.0 wt%). The size and density of scatterers are among the factors that determine the scattering attenuation and the echo intensity at each observation depth. A scatterer diameter of 10 µm was used to assess the effect of scattering in small scatterers, assuming a single hepatic cell size (i.e., approximately 10 µm [34]). This phantom mimicked the situation where a single cell nucleus is assumed to be the dominant scattering source. The scatterer diameter of 40 µm was used to examine the effect of scattering from large scatterers or a cluster of scattering sources, assuming a microstructure in which a few tissue types were mixed, or a tissue that was larger than a single cell and had strong backscattering such as lipid droplets. Note that these two phantoms intended to mimic only the scatterer size of the material (i.e., did not replicate the acoustical properties of hepatocytes or lipid droplets) since the materials of the two types of scatterers were the same. 40 wt% evaporated milk [35] was added to the same recipe as phantoms I–III to adjust the absorption attenuation of the material [36] (phantoms VII–IX). These mimicked more practical circumstances with scattering from a smaller scattering source and absorption attenuation. Measurements were also taken for five different ratios of evaporated milk to water (20, 40, 60, 80, and 100 wt%) to confirm the acoustic properties of evaporated milk.

Ex vivo rat livers

Two (one normal and one fatty liver model) 8-week-old male rats (Slc:SD) were enrolled in this study. Livers were enucleated from a normal model fed with a normal diet (Lab MR Stock; Nosan, Kanagawa, Japan) and a fatty liver model fed with a high-fat and cholesterol diet (HFC; Funabashi Farm, Chiba, Japan). Post-enucleation, the largest

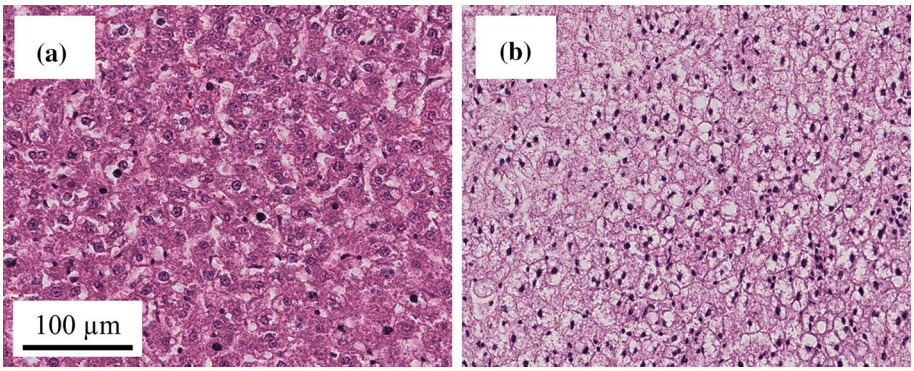

Fig. 1 Images of hematoxylin–eosin staining of livers of normal liver model rat (**a**), and fatty liver model rat (**b**)

liver lobe was trimmed for further observation. Figure 1 shows pathology images of hematoxylin–eosin staining from the same sample after ultrasound observation. In the normal liver model rat, hepatocytes that can be considered the main scattering source were distributed densely and homogeneously (Fig. 1a). In the fatty liver model rat, hepatocytes and lipid droplets were distributed concurrently throughout the image (Fig. 1b). Lipid droplets were considered the main scattering source in the fatty liver. This means that the main scatterers were larger in fatty liver than in normal liver. This animal experiment protocol was approved by the animal experiment committee of Chiba University.

Data acquisition using laboratory-made scanners

In this study, data were acquired using transducers with five different frequency characteristics. The three-dimensional (3D) RF echo signal of each phantom was acquired with a custom-made ultrasonic scanner [37] with five single-element concave transducers. A commercialized pulser/receiver (Model 5800; OLYMPUS, Tokyo, Japan) was employed to excite the transducers. Supplementary Table 2 summarizes the focal depth and aperture diameter for each transducer, the energy levels of the pulser, and the cut-off frequencies of the low- and high-pass filters in the receiver in each transducer. The RF echo signals were digitized with the sampling frequency of 100 MHz and 12 bits of accuracy using an oscilloscope (HDO6104; LeCroy, NY, USA). Each target (i.e. phantoms or dissected livers) was placed on an acrylic plate settled in a water tank filled with degassed water at 22 ℃. Polyvinylidene chloride film wrap was attached on the surface of the target to clarify the surface reflection. For the measurement of evaporated milk, degassed water and evaporated milk (i.e. 22 ℃) were placed separately in a tank with a fixed acrylic plate. In this case, the distance between the acrylic plate and the transducer was the same. The transducer was mechanically scanned in the horizontal directions along the three-axis linear motor stages (MTN100CC; Newport, CA, USA). For phantom measurement, the RF signal was acquired at every 100-µm interval horizontally. The volume of the 3D RF data was 2048 × 31 × 21 pixels (depth direction × horizontal directions) under the center frequency of 5 MHz, and 4096 × 31 × 21 pixels over the center frequency of 10 and 15 MHz. For rat liver measurements, the RF signal was acquired at every 1000-µm interval horizontally. The volume of the 3D RF data was 2048 × 3 × 2 pixels (depth direction × horizontal directions) under the center frequency of 5 MHz, and 4096 × 3 × 2 pixels over the center frequency of 10 and 15 MHz. These gate lengths of echo data included depth from the surfaces of the targets to the acrylic plate (bottom of the targets).

Methods for speed of sound and attenuation coefficient evaluation

The SoS and the attenuation coefficient of each phantom were evaluated using the reflector model [38]. Two independent RF echo signals, RF_p and RF_{ref}, in the measurements with and without the phantom were observed, respectively. SoS evaluation was based on the equation $C_{ref}\left(t_{ref}-t_{p1}\right)/\left(t_{p2}-t_{p1}\right)$. In this equation, t_{p1} and t_{p2} were the time-of-flight from the transducer to the phantom surface and to the reflector surface, respectively. t_{ref} was the time-of-flight from the transducer to the reflector surface without the phantom. Each parameter was defined as the propagation peak-to-peak delay times. C_{ref} was the SoS in degassed water at 22 ℃ and was fixed at 1489 m/s.

The total attenuation in the phantom, α_p [dB/cm], was calculated from the normalized power spectrum as follows:

$$\alpha_p(f,d)=\frac{8.686\log_{\mathrm{e}}\left[\frac{S_p(f,d)}{S_{\mathrm{ref}}(f,d)}\right]}{2d}, \tag{1}$$

where S_p and S_{ref} were the power spectra of echoes from the phantom–reflector boundary and the degassed water–reflector without the phantom, respectively. f and d were the center frequency and depth position, respectively. Finally, the attenuation coefficient α_0 was computed as the slope of the linear equation $\alpha_p(f)=\alpha_0 f^1+b$ using the

least-squares method. The frequency bandwidth (approximately –6 dB) for each transducer is summarized in Supplementary Table 2.

Results and discussion

Characteristics of speed of sound in nine phantoms

Figure 2a illustrates average and standard deviation of the SoS estimated from the nine phantoms with various densities of scatterers, scatterer sizes, or absorption attenuations evaluated at the center frequency of 1, 3.5, 5, 10, or 15 MHz. No significant change in the SoS for the same phantom was confirmed among the frequencies. These results were consistent with the experimental values of SoS presented by Brewin et al. evaluated in the frequency range of 17–23 MHz [39] and Sun et al. evaluated over the frequency range of 10–47 MHz [40]. Among the densities of the scatterer, the estimated SoS increased as the densities of the scatterer increased. The increase in SoS with the increment of scatterer density was comparable between the two types of scatterers (i.e., 1.16% in the 10-μm phantom vs 1.02% in the 40-μm phantom). Matsukawa et al. [41] reported the effects of scatterer size and density on ultrasonic properties in the range of 1–30 MHz. They concluded that the SoS decreased with increasing scatterer density for a diameter of 4 μm or less (e.g., talc and graphite), while the SoS was stable or marginally increased with increasing scatterer density for a diameter of 12.3 μm or greater (e.g., graphite and glass beads). The scatterers used in the present study were made of nylon with a diameter of 10 or 40 μm, which is consistent with their results.

Between the phantoms with different scatterer sizes (i.e., phantoms I and IV, II and V, and III and VI), little difference in SoS was confirmed (2.39 m/s for I and IV, 1.97 m/s for II and V, and 3.27 m/s for III and VI on average, respectively). This is possibly attributed to the same proportion of scatterers between the phantoms despite their different scatterer sizes. However, since the dispersion of the evaluation of SoS tends to be larger with a larger scatterer diameter, a larger scatterer diameter is considered to be more susceptible to local scattering in the ultrasonic transmission/reception path. Matsukawa et al. reported that the SoS increased as a function of frequency (from 1 to 30 MHz) dependent on the scatterer size, stiffness, and base gel viscosity [42]. They concluded that it was because the scattering loss became dominant when the diameter of the scatterers increased. The difference between their result and ours is presence or absence of viscosity.

In comparison with the phantoms with different absorption attenuations in the same scatterer densities and scatterer sizes (i.e., phantoms I and VII, II and VIII, and III and IX), the difference in SoS was approximately 20 m/s for all of the phantoms, regardless of the density of the scatterer (22.1 m/s for I and VII, 22.4 m/s for II and VIII, and 21.2 m/s for III and IX on average, respectively). Figure 2b shows the estimated SoS of the various ratios of evaporated milk and degassed water (i.e. 20–100 wt%) at 1 to 15 MHz. A linear correlation was confirmed between the SoS and the density of evaporated milk. The relationship between the percentage of evaporated milk to water and the SoS was consistent with the experimental values evaluated at 1 MHz by means of the transmission method reported by Farrer et al. [43]. Considering the SoS of water at 22 ℃ (i.e., 1,489 m/s) and the measured SoS of 40 wt% evaporated milk (i.e., 1,545.29 m/s on average, Fig. 2b), the SoS of the evaporated milk is considered to be the dominant factor for the SoS of phantoms VII–IX (Fig. 2a).

Characteristics of attenuation coefficient in nine phantoms

Figure 3a shows the attenuation coefficient of phantoms evaluated at 1–15 MHz. The attenuation coefficient of all phantoms increased with increased frequency, except

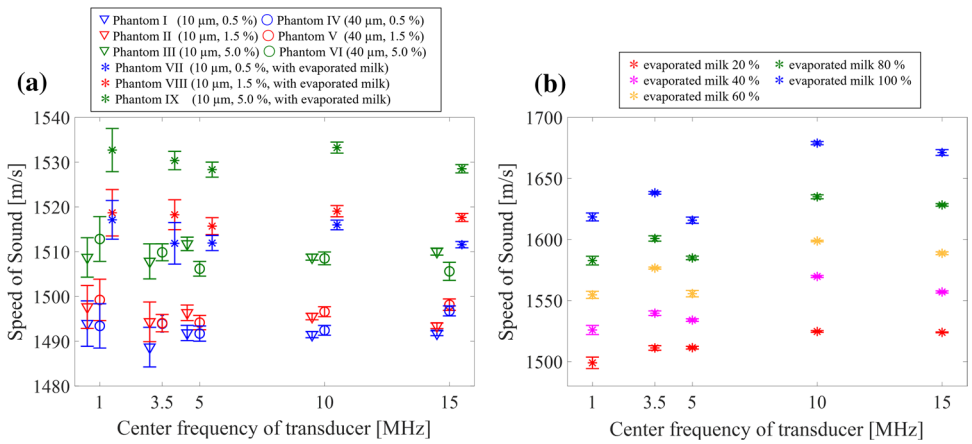

Fig. 2 Speed of sound of phantoms (**a**) and prepared mediums with a ratio of evaporated milk to water of 20–100 wt% (**b**) evaluated at 1–15 MHz. Error bars represent the standard deviation

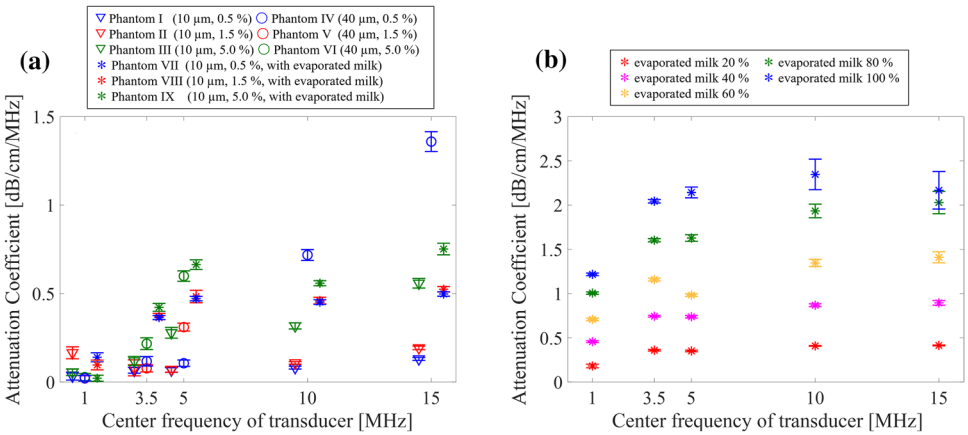

Fig. 3 Average and standard deviation of attenuation coefficients of phantoms (**a**) and prepared mediums with a ratio of evaporated milk to water of 20 to 100 wt% (**b**) evaluated at 1 to 15 MHz

for phantom II at 1 MHz. The attenuation coefficient was approximately 0.19 dB/cm/MHz higher on average in accordance with the increasing density of scatterers (from 0.5% to 5%). This trend was in agreement with the result shown by Inglis et al., who evaluated attenuation coefficients in the frequency range of 7.5–12 MHz, although they used different scatterers (Al_2O_3 and SiC particles) [44]. Among the phantoms with different scatterer sizes, the phantoms containing the 40-μm-diameter scatterers (phantoms IV, V, and VI) showed higher attenuation coefficients than those containing the 10-μm-diameter scatterers (phantoms I, II, and III). This trend was specifically prominent at high frequencies (i.e., 10 MHz to 15 MHz). This implies an increase in scattering loss in the phantom, which agrees with the previous studies [42, 45].

Among the phantoms with different media, the phantoms containing evaporated milk (phantoms VII–IX) showed higher attenuation coefficients than those containing only water as media (phantoms I–III). These differences possibly derive from the difference in absorption attenuation of the media based on a previous study done by Drakos et al. [34]. Note that phantoms VII–IX contain absorption materials only, whereas phantoms I–III have both absorption and scattering materials. Figure 3b shows the attenuation coefficient of the mixture of evaporated milk and water evaluated at 1–15 MHz to verify this assumption. The averaged difference in attenuation coefficients at each frequency was 0.34 dB/cm/MHz between the phantom containing 40 wt% evaporated milk + 0.5 wt% spherical nylon scatterers (phantom VII) and 40 wt% evaporated milk alone. This suggests that the attenuation coefficient of the media dominates the attenuation coefficient of the phantom. Our results showing the changes in the attenuation coefficient with the presence of evaporated milk was consistent with the trends of solid evaporated milk with different volume fractions shown by Madsen et al. [46].

Another examination was performed to determine the more dominant attenuation phenomena (i.e., absorption or scattering attenuation) in each phantom. Figures 4a-1, a-2, a-3 show the attenuation of phantoms as a function of frequency.

Attenuation is subdivided into three definitions: diffusion attenuation due to the geometrical spread of acoustic waves, absorption attenuation due to the conversion of the power of acoustic waves into heat, and scattering attenuation due to the inhomogeneity of the material. The following equation describes the amount of attenuation. When $n = 1$, the equation means the attenuation of the medium describes absorption attenuation only:

$$\alpha = \alpha_p f^n. \tag{2}$$

Figures 4a-1 and a-3 show the phantoms containing scatterers of the same scatterer size (i.e., 10-μm scatterers). The phantoms containing evaporated milk (phantoms VII to IX, Fig. 4a-3) showed higher attenuation with linear frequency dependence. Higher attenuation means that absorption attenuation dominates the attenuation of the evaporated milk according to the assessment in the previous sections. Since the plots as a function of frequency were nearly linear, n was estimated to be closer to 1 as the total attenuation (i.e., absorption > > scattering > > diffusion). On the other hand, the attenuation of the phantoms containing 40-μm scatterers (Fig. 4a-2) showed a significantly different trend. This was because the multiplier n was larger than 1 due to larger scatterers, and changed non-linearly. As reported by Sato et al. [45], a larger scatterer diameter causes non-linear changes as a function of frequency (i.e. n > 1). Our results are also consistent with the results with low frequencies reported by Sun et al. [40] and Browne et al. [47].

Figure 4b-1, b-2, b-3 shows examples of the spectrum of the echo signal from the phantoms and reference material (acrylic plate) with the 1.5 wt% density of scatterers [(b-1): Phantom II, (b-2): Phantom V, (b-3): Phantom VIII] observed at 15 MHz. Figure 4c-1, c-2, c-3 shows the subtraction of the phantom and the reference spectrum. The

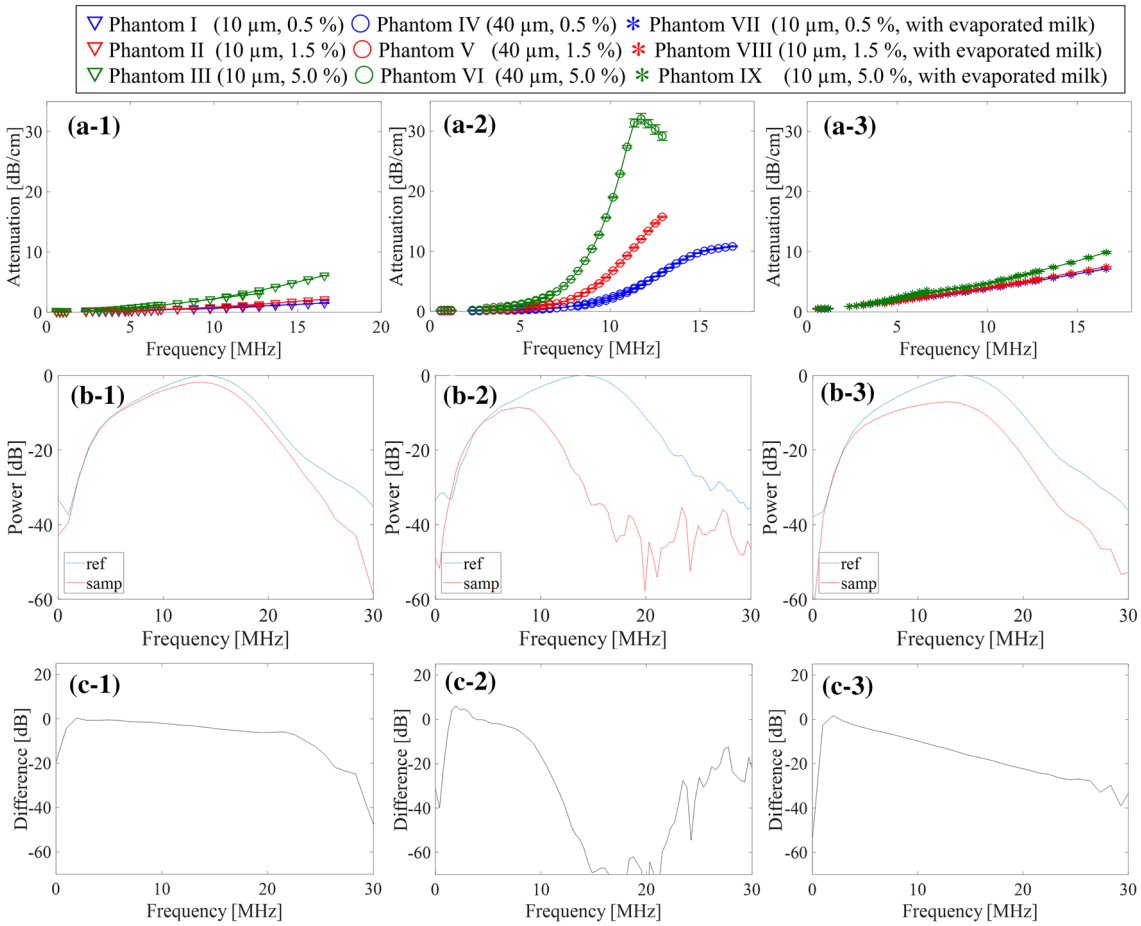

Fig. 4 Average and standard deviation of attenuation of phantoms I-III (**a**-1), IV-VI (**a**-2), and VII-IX (**a**-3). Representative frequency characteristics of echo signals of phantom II (**b**-1), phantom V (**b**-2), and phantom VIII (**b**-3) at 15 MHz. Blue lines show the power of the reflected signal from the acrylic plate without the phantom, and red lines show the power of the reflected signal from the acrylic plate via the phantom. Difference in the power in phantom II (**c**-1), phantom V (**c**-2), and phantom VIII (**c**-3)

spectrum power with the phantoms containing evaporated milk (Fig. 4b-3 and c-3) decreased linearly by 10 MHz as a function of the frequency in comparison with the phantom only containing the scatterer (Fig. 4b-1, c-1, b-2, and c-2).

These results suggested that the frequency dependence in the attenuation coefficient was less strong with a smaller scatterer diameter (i.e., 10 µm), while the larger scatterers (i.e., 40 µm) had a stronger frequency dependence. This difference is possibly means that only scattering attenuation occurs in these phantoms, and the degree of scattering is weaker with the smaller scatterer diameter. In addition, the presence of absorption attenuation-caused media results in a steeper linear slope in the frequency dependence regardless of the presence of scattering attenuation. In other words, understanding these relationships will allow us to analogize the ratio of absorption attenuation to scattering attenuation in the evaluation medium. However, the size of the main scatterers in the target area must be estimated prior to this analogization.

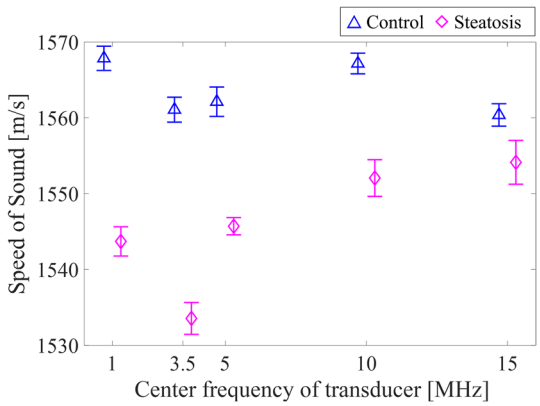

Fig. 5 Average and standard deviation of speed of sound of livers of normal liver model (blue triangle) rat and fatty liver model (magenta diamond) rat measured at each frequency

Characteristics of speed of sound in rat liver

Figure 5 shows the estimated SoS of the rat liver displaying the slower SoS with the fatty liver as compared to the normal liver. This trend was consistent with a previous study with evaluation at 3.5 MHz (Hachiya et al. [32]) despite the difference in the measurement temperature (37 ℃ for their results and 22 ℃ for our results).

The composition of normal liver from an acoustical perspective is similar to that of phantoms VII, VIII, and IX, which contain 10-µm-diameter scatterers and evaporated milk. That is, both contain small scatterers and have viscous properties. As shown in the phantom study, the SoS of the mixed material was greatly affected by the media (i.e., water or evaporated milk) when the scatterer was small. Thus, it can be assumed that in the normal liver, the SoS of the liver parenchyma (with absorption attenuation), which encompasses small scatterers, mainly cell nuclei, is being evaluated. The fatty liver has multiple scatterers with different diameters, acoustic impedances, and viscoelasticity. Considering the results from the phantoms with different scatterer diameters, slower SoS in the fatty liver is mainly caused by lower scatterer density and slower SoS of the lipid droplets. SoS evaluation of the lipid droplets is expected to unveil further details of this observation.

Characteristics of attenuation coefficient in rat liver

Figure 6 shows the attenuation coefficients of normal and fatty rat liver. The results from the fatty liver showed a higher mean attenuation coefficient as well as a steeper frequency dependence slope. Figure 7 shows the attenuation, frequency characteristics, and difference in the power of the rat livers. The characteristics of the echo signal of the normal liver (Fig. 7a-1, b-1, and c-1) were similar to the results of the phantoms with a mixture of evaporated milk and 10-µm-diameter scatterers (Fig. 4a-3, b-3, and c-3). In other words, absorption attenuation can be dominant in the normal liver with smaller scatterers, but the scattering attenuation was also mixed to some extent.

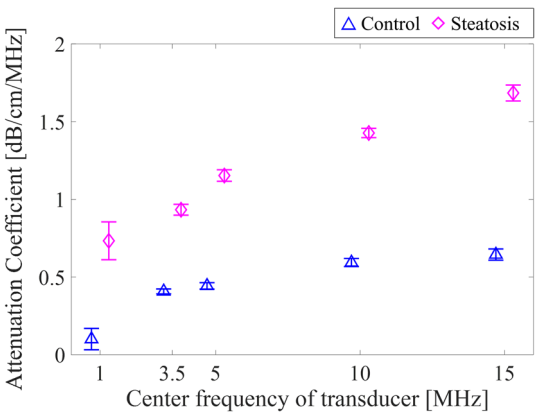

Fig. 6 Average and standard deviation of attenuation coefficients of livers of normal liver model rat (blue triangle) and fatty liver model rat (magenta diamond) measured at each frequency

The echo signal characteristics of fatty liver (Fig. 7a-2, b-2, and c-2) showed a trend toward steep changes in the attenuation coefficient as a function of frequency, which was similar to the phantoms with a larger scatterer diameter (Fig. 4a-2, b-2, and c-2). However, the linearity of the attenuation decreases with frequency was stronger than that for phantoms IV, V, and VI. This indicates that lipid droplets can also be a scattering source with a larger diameter, and the reflections and interference from them determine the characteristics of the echo signal; the scattering attenuation is considered dominant in this case. However, the characteristic change is not as drastic as that with the phantoms since the absorption attenuation originally possessed by the liver is also retained.

Conclusion

The results showed that the density of scatterers and the SoS of the base medium affected the SoS of the phantom regardless of the size of scatterers. Frequency dependence of the SoS was not observed in any of the phantoms. Regarding attenuation coefficient, the frequency dependence of the attenuation coefficient strongly depended on the absorption attenuation, which was peculiar to the medium, size, and density of the scatterers. Different changes occurred according to the respective attenuation characteristics assumed in actual living tissues. These experiments with the phantom and rat liver allowed us to consider in detail the effects of scattering and absorption on the tissue-specific acoustic properties of the target. A systematic database is needed as a reference to allows us to accurately estimate the contribution of both attenuation characteristics. Numerical simulations can also help to evaluate absorption and scattering attenuation as absolute quantities. However, remarkably microscopic phenomena such as internal heating in absorption attenuation are presumably challenging to explore both by actual measurements and by simulations. In addition, characteristic evaluation using high-frequency ultrasound of 25–50 MHz will certainly become essential as these frequency bands are being implemented in clinical ultrasonic diagnostic equipment in recent years. The fundamental challenge in these studies is the need to create extremely thin phantoms considering the large attenuation of the target medium. Addressing this issue will enable interoperability with acoustic property results from acoustic microscopy above 100 MHz.

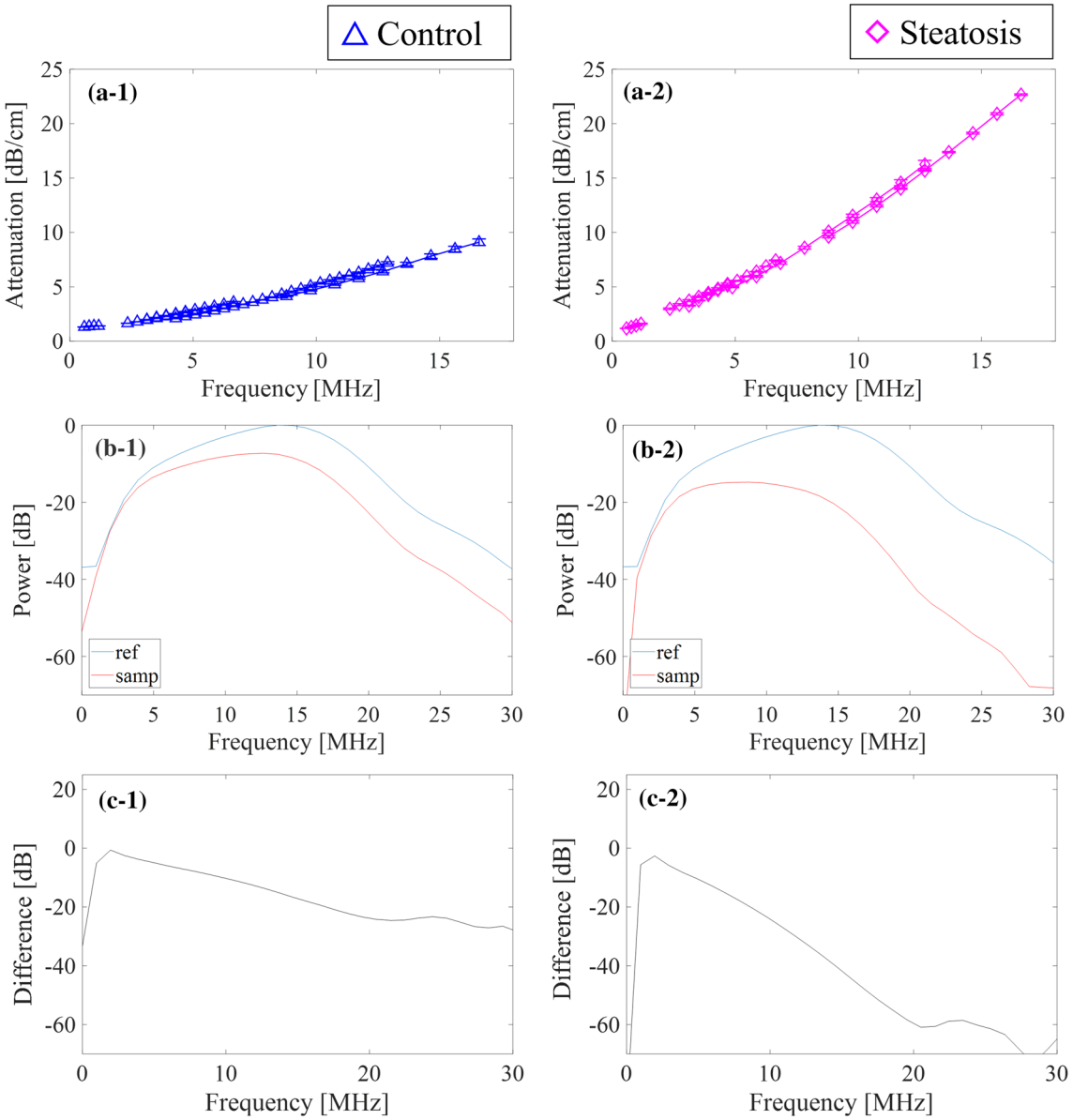

Fig. 7 Average and standard deviation of attenuation of livers of normal liver model rat (**a**-1) and fatty liver model rat (**a**-2), frequency characteristics of livers of normal liver model rat (**b**-1) and fatty liver model rat (**b**-2), and difference in the power of normal liver model rat (**c**-1) and fatty liver model rat (**c**-2)

Supplementary Information The online version contains supplementary material available at https://doi.org/10.1007/s10396-022-01235-1.

Acknowledgements This work was partly supported by JSPS Core-to-Core Program JPJSCCA20170004, and KAKENHI Grant Number 19H04482. We also acknowledge financial support from the Institute for Global Prominent Research at Chiba University.

Declarations

Conflict of interest The authors declare that there are no conflicts of interest.

Ethical statements All institutional and national guidelines for the care and use of laboratory animals were followed.

References

1. Yamaguchi T. Basic concept and clinical applications of quantitative ultrasound (QUS) technologies. J Med Ultrason. 2021;48:391–402.

2. Ophir J, Céspedes I, Ponnekanti H, et al. Elastography: A quantitative method for imaging the elasticity of biological tissues. Ultrason Imaging. 1991;13:111–34.
3. Harada N, Shirabe K, Ijichi H, et al. Acoustic radiation force impulse imaging predicts postoperative ascites resulting from curative hepatic resection for hepatocellular carcinoma. Surgery. 2012;151:837–43.
4. Zhang P, Zhou P, Tian SM, et al. Application of acoustic radiation force impulse imaging for the evaluation of focal liver lesion elasticity. Hepatobiliary Pancreat Dis Int. 2013;12:165–70.
5. Kitazaki T, Kondo K, Yamakawa M, et al. Shear wavelength estimation based on inverse filtering and multiple-point shear wave generation. Jpn J Appl Phys. 2016. https://doi.org/10.7567/JJAP.55.07KF10.
6. Zhi H, Xiao XY, Ou B, et al. Could ultrasonic elastography help the diagnosis of small (≤2 cm) breast cancer with the usage of sonographic BI-RADS classification? Eur J Radiol. 2012;81:3216–21.
7. Choi WJ, Kim HH, Cha JH, et al. Predicting prognostic factors of breast cancer using shear wave elastography. Ultrasound Med Biol. 2014;40:269–74.
8. Feleppa E, Kalisz A, Sokil-Melgar JB, et al. Typing of prostate tissue by ultrasonic spectrum analysis. IEEE Trans Ultrason Ferroelectr Freq Control. 1996;43:609–19.
9. Mamou J, Coron A, Oelze ML, et al. Three-dimensional high-frequency backscatter and envelope quantification of cancerous human lymph nodes. Ultrasound Med Biol. 2011;37:345–57.
10. Oelze ML, O'Brien WD, Blue JP, et al. Differentiation and characterization of rat mammary fibroadenomas and 4T1 mouse carcinomas using quantitative ultrasound imaging. IEEE Trans Med Imaging. 2004;23:764–71.
11. Higuchi T, Hirata S, Yamaguchi T, et al. Liver tissue characterization for each pixel in ultrasound image using multi-Rayleigh model. Jpn J Appl Phys. 2014. https://doi.org/10.7567/JJAP.53.07KF27.
12. Igarashi Y, Ezuka H, Yamaguchi T, et al. Quantitative estimation method for liver fibrosis based on combination of Rayleigh distributions. Jpn J Appl Phys. 2010. https://doi.org/10.1143/JJAP.49.07HF06.
13. Nakajima S, Shibuya K, Kamiyama N, et al. Comparison of ultrasound colored image views produced by application of statistical analysis of radio-frequency signals and histological findings in patients with chronic hepatitis C. J Med Ultrason. 2010;37:51–8.
14. Ricci P, Marigliano C, Cantisani V, et al. Valutazione ecografica della fibrosi epatica: esperienza preliminare con acoustic structure quantification (ASQ). Radiol Medica. 2013;118:995–1010.
15. Yamaguchi T, Hachiya H. Proposal of a parametric imaging method for quantitative diagnosis of liver fibrosis. J Med Ultrason. 2010;37:155–66.
16. Yu I, Yamaguchi T, Hachiya H. Stability of quantitative evaluation method of liver fibrosis using amplitude distribution model of fibrotic liver. Jpn J Appl Phys. 2011. https://doi.org/10.7567/JJAP.50.07HF17.
17. Fujii Y, Taniguchi N, Takano R, et al. Texture analysis with a new method in which the region of interest is segmented into multiple layers for radiofrequency amplitude histogram analysis of fibrous rat livers. J Med Ultrason. 2004;31:13–20.
18. Kaltenbach TEM, Gruener B, Akinli AS, et al. Acoustic structure quantification (ASQ): a new tool in sonographic examination of liver lesions in hepatic alveolar echinococcosis. J Med Ultrason. 2014;41:445–53.
19. Ghoshal G, Lavarello RJ, Kemmerer JP, et al. Ex vivo study of quantitative ultrasound parameters in fatty rabbit livers. Ultrasound Med Biol. 2012;38:2238–48.
20. Tamura K, Mamou J, Yoshida K, et al. Ultrasound-based lipid content quantification using double Nakagami distribution model in rat liver steatosis. Jpn J Appl Phys. 2020. https://doi.org/10.35848/1347-4065/ab918e.
21. Sasso M, Audière S, Kemgang A, et al. Liver steatosis assessed by controlled attenuation parameter (CAP) measured with the XL probe of the fibroscan: a pilot study assessing diagnostic accuracy. Ultrasound Med Biol. 2016;42:92–103.
22. Audière S, Labourdette A, Miette V, et al. Improved ultrasound attenuation measurement method for the non-invasive evaluation of hepatic steatosis using fibroscan. Ultrasound Med Biol. 2021;47:3181–95.
23. Tamaki N, Koizumi Y, Hirooka M, et al. Novel quantitative assessment system of liver steatosis using a newly developed attenuation measurement method. Hepatol Res. 2018;48:821–8.
24. Weijers G, Starke A, Thijssen JM, et al. Transcutaneous vs. intraoperative quantitative ultrasound for staging bovine hepatic steatosis. Ultrasound Med Biol. 2012;38:1404–13.
25. Ogawa T, Yoshida K, Yamaguchi T. Speed of sound evaluation considering spatial resolution in a scanning acoustic microscopy system capable of observing wide spatial area. Jpn J Appl Phys. 2020. https://doi.org/10.35848/1347-4065/ab83da.
26. Abe K, Arakawa M, Kanai H. Estimation method for sound velocity distribution for high-resolution ultrasonic tomographic imaging. J Med Ultrason. 2019;46:27–33.
27. Imbault M, Faccinetto A, Osmanski BF, et al. Robust sound speed estimation for ultrasound-based hepatic steatosis assessment. Phys Med Biol. 2017;62:3582–98.
28. Tsujimoto Y, Matsuda D, Minamiguchi K, et al. Measurement of temperature dependence of sound velocity in biological tissues. Jpn J Appl Phys. 2019. https://doi.org/10.7567/1347-4065/ab12cb.
29. Hasegawa H, Nagaoka R. Initial phantom study on estimation of speed of sound in medium using coherence among received echo signals. J Med Ultrason. 2019;46:297–307.
30. Goss SA, Johnston RL, Dunn F. Comprehensive compilation of empirical ultrasonic properties of mammalian tissues. J Acoust Soc Am. 1978;64:423–57.
31. Hachiya H, Ohtsuki S, Tanaka M. Relationship between speed of sound in and density of normal and diseased rat livers. Jpn J Appl Phys. 1994;33:3130–3.
32. Hachiya H, Yamaguchi T. Acoustic characteristics of the tissue and the ultrasonic B-mode Image. Med Imaging Technol. 2003;21:95–100 (**[in japanese]**).
33. Irie S, Inoue K, Yoshida K, et al. Speed of sound in diseased liver observed by scanning acoustic microscopy with 80 MHz and 250 MHz. J Acoust Soc Am. 2016;139:512–9.
34. Strohm EM, Moore MJ, Kolios MC. Single cell photoacoustic microscopy: a review. IEEE J Sel Top Quantum Electron. 2016;22:137–51.
35. Drakos T, Antoniou A, Evripidou N, et al. Ultrasonic attenuation of an agar, silicon dioxide, and evaporated milk gel phantom. J Med Ultrasound. 2021;29:239–49.
36. Drakos T, Giannakou M, Menikou G, et al. An improved method to estimate ultrasonic absorption in agar-based gel phantom using thermocouples and MR thermometry. Ultrasonics. 2020;103:106089.
37. Omura M, Yoshida K, Akita S, et al. Verification of echo amplitude envelope analysis method in skin tissues for quantitative follow-up of healing ulcers. Jpn J Appl Phys. 2018. https://doi.org/10.7567/JJAP.57.07LF15.
38. Schwartz M. Estimating the acoustic attenuation coefficient slope for liver from reflected ultrasound signals. IEEE Trans Sonics Ultrason. 1979;26:353–61.
39. Brewin MP, Pike LC, Rowland DE, et al. The acoustic properties, centered on 20 MHZ, of an IEC agar-based tissue-mimicking material and its temperature, frequency and age dependence. Ultrasound Med Biol. 2008;34:1292–306.

40. Sun C, Pye SD, Browne JE, et al. The speed of sound and attenuation of an IEC agar-based tissue-mimicking material for high frequency ultrasound applications. Ultrasound Med Biol. 2012;38:1262–70.
41. Matsukawa M, Akimoto T, Ueba S, et al. Ultrasonic wave properties in the particle compounded agarose gels. Ultrasonics. 2002;40:323–7.
42. Matsukawa M, Sasaki K, Akimoto T, et al. Application of a suspension theory to particle-dispersed agarose gels. Jpn J Appl Phys. 2002;41:3163–7.
43. Farrer AI, Odéen H, de Bever J, et al. Characterization and evaluation of tissue-mimicking gelatin phantoms for use with MRgFUS. J Ther Ultrasound. 2015;3:1–11.
44. Inglis S, Ramnarine KV, Plevris JN, et al. An anthropomorphic tissue-mimicking phantom of the oesophagus for endoscopic ultrasound. Ultrasound Med Biol. 2006;32:249–59.
45. Sato T, Watanabe Y. High sensitivity estimation of red blood cell aggregation with ultrasonic peak frequency. IEEE International Ultrasonics Symposium (IUS). 2013. pp 868–71.
46. Madsen EL, Frank GR, Dong F. Liquid or solid ultrasonically tissue-mimicking materials with very low scatter. Ultrasound Med Biol. 1998;24:535–42.
47. Browne JE, Ramnarine KV, Watson AJ, et al. Assessment of the acoustic properties of common tissue-mimicking test phantoms. Ultrasound Med Biol. 2003;29:1053–60.